Memory of shear flow in soft jammed materials

H. A. Vinutha [ID][a,*], Manon Marchand [ID][b], Marco Caggioni [ID][c], Vishwas V. Vasisht [ID][d], Emanuela Del Gado [ID][a,*] and Veronique Trappe [ID][b,*]

[a]Department of Physics, Institute for Soft Matter Synthesis and Metrology, Georgetown University, Washington, DC, USA
[b]Department of Physics, University of Fribourg, Fribourg, Switzerland
[c]Complex Fluid Microstructures, Corporate Engineering, Procter & Gamble Company, West Chester, OH 45069, USA
[d]Department of Physics, Indian Institute of Technology Palakkad, Nila Campus, Kanjikode, Palakkad, Kerala 678623, India
*To whom correspondence should be addressed: Email: vh163@georgetown.edu (H.A.V); ed610@georgetown.edu (E.D.G.); veronique.trappe@unifr.ch (V.T.)
Edited By Gary Grest

Abstract

Cessation of flow in yield stress fluids results in a stress relaxation process that eventually leads to a finite residual stress. Both the rate of stress relaxation and the magnitude of the residual stresses systematically depend on the preceding flow conditions. To assess the microscopic origin of this memory effect, we combine experiments with large-scale computer simulations, exploring the behavior of jammed suspensions of soft repulsive particles. A spatiotemporal analysis of particle motion reveals that memory formation during flow is primarily governed by the emergence of domains of spatially correlated nonaffine displacements. These domains imprint the configuration of stress imbalances that drive dynamics upon flow cessation, as evidenced by a striking equivalence of the spatial correlation patterns in particle displacements observed during flow and upon flow cessation. Additional contributions to stress relaxation result from the particle packing that reorganizes to minimize the resistance to flow by decreasing the number of locally stiffer configurations. Regaining rigidity upon flow cessation drives further relaxation and effectively sets the magnitude of the residual stress. Our findings highlight that flow in yield stress fluids can be seen as a training process during which the material stores information of the flowing state through the development of domains of correlated particle displacements and the reorganization of particle packings optimized to sustain the flow. This encoded memory can then be retrieved in flow cessation experiments.

Keywords: yield stress fluid, soft jammed materials, flow cessation, memory of flow, correlated dynamics

---

Significance Statement

The mechanical properties of yield stress fluids are well known to depend on their shear history. A striking example of history dependence is observed in flow cessation tests, where stress relaxation upon stopping the flow systematically depends on the previous flow conditions. We here combine experiments and simulations to investigate the origin of such flow memory in jammed packings of soft particles. Our research reveals that shear flow both imprints a memory of spatial correlations in the dynamics of neighboring particles and decreases the mechanical stability of the system. Both aspects set the conditions for stress relaxation upon cessation of flow.

Soft jammed materials are suspensions of soft, deformable particles that are packed above the jamming transition. At these concentrations, the particles are in contact, interacting elastically with each other, and the material classifies as a weak solid. Despite its intrinsic solid properties, a soft jammed material can be continuously sheared without fracturing, which generates a stress (σ) that is above a threshold stress, known as the dynamic yield stress (σ_y). Indeed, soft jammed materials belong to a broader class of materials called yield stress fluids (1, 2), which encompasses foams, creams, cement paste, etc. The use of these systems generally relies on their ability to flow under the application of either, a large enough stress or a constant shear rate (3–5). This is why they can be conveniently pumped through pipes, squeezed out of tubes, spread on surfaces, and/or molded into a given shape.

To explore the consequences of flow history on the properties of yield stress fluids, experiments and simulations have been devised to measure stress relaxation upon flow cessation (6–16). This test consists of first driving the system to a steady flow state, where the stress remains constant in time. The strain rate is then set to zero, the strain maintained constant, and stress relaxation measured as a function of time. Both the time scales of stress relaxation as well as the final residual stress reached at the end of the relaxation process have been found to depend on the shear parameters setting the flow conditions prior to flow cessation (6, 7, 9). Distinct particle dynamics and structural rearrangements have been shown to contribute to stress relaxation (6, 7). However, the pathway through which information of flow is stored into the system to then result in a

specific stress relaxation pattern upon flow cessation is still not understood.

In this contribution, we explore this phenomenon combining experiments and simulations using highly packed systems of soft particles suspended in a continuous medium of varying viscosity. Our investigations reveal that flow encodes a memory of two processes. The first one relates to the system's response to the continuously increasing strain by forming domains that extend over several particle diameters. Within these domains elastic energy is stored, evidenced by short-time nonaffine particle displacements that are both directed and highly correlated within the domains. This process depends on shear rate and is independent of the viscosity of the suspending medium. The elastic load is isotropic, but locally unbalanced, leading upon flow cessation to fast quasiballistic displacements that exhibit spatial correlations mirroring those observed under flow. The second process relates to a reconfiguration of the particle packing under flow, which leads to locally less stiff configurations, the overall stiffness being a function of the viscous stress experienced during flow. Upon flow cessation the particle packing evolves during stress relaxation until it reaches a rigidity level that satisfies the conditions of mechanical stability; the time scale to reach this condition then sets the magnitude of residual stress. Our findings effectively disclose the origin of flow memory observed upon flow cessation and expose that flow cessation tests are efficient means to gain insight into the flow behavior of yield stress fluids.

As introduced above, our aim is to address how the application of a continuous shear rate imprints memory into a soft jammed material. To gain an understanding of the effect of the shear rate applied independently of the resulting stress, we explore the flow behavior of a densely packed microgel system composed of Carbopol dispersed in propylene glycol and vary the viscosity of the dispersing medium by varying the temperature. As shown in the main graph of Fig. 1a, our system exhibits the typical flow characteristics of a simple yield stress fluid. While the stress increases monotonically in the range of high shear rates, the stress is almost shear rate independent at low shear rates. Clearly, the system can only sustain a steady flow when the stress exceeds the dynamic yield stress σ_y, defined as the value of stress in the limit of $\dot{\gamma} \to 0$. The yield stress is independent of the solvent viscosity, which denotes that σ_y is exclusively set by the intrinsically solid characteristics of the dense particle ensemble. By contrast, the stress sensitively depends on the solvent viscosity η_s at higher shear rates. For a given shear rate the stress increases with increasing η_s, which reflects that the stress generated at finite shear rates also depends on viscous dissipation in the continuous phase (17).

To gain insight in the shear rate-dependent states, we perform flow cessation experiments at various shear rates along the flow curve. These tests consist of stopping the shear after reaching
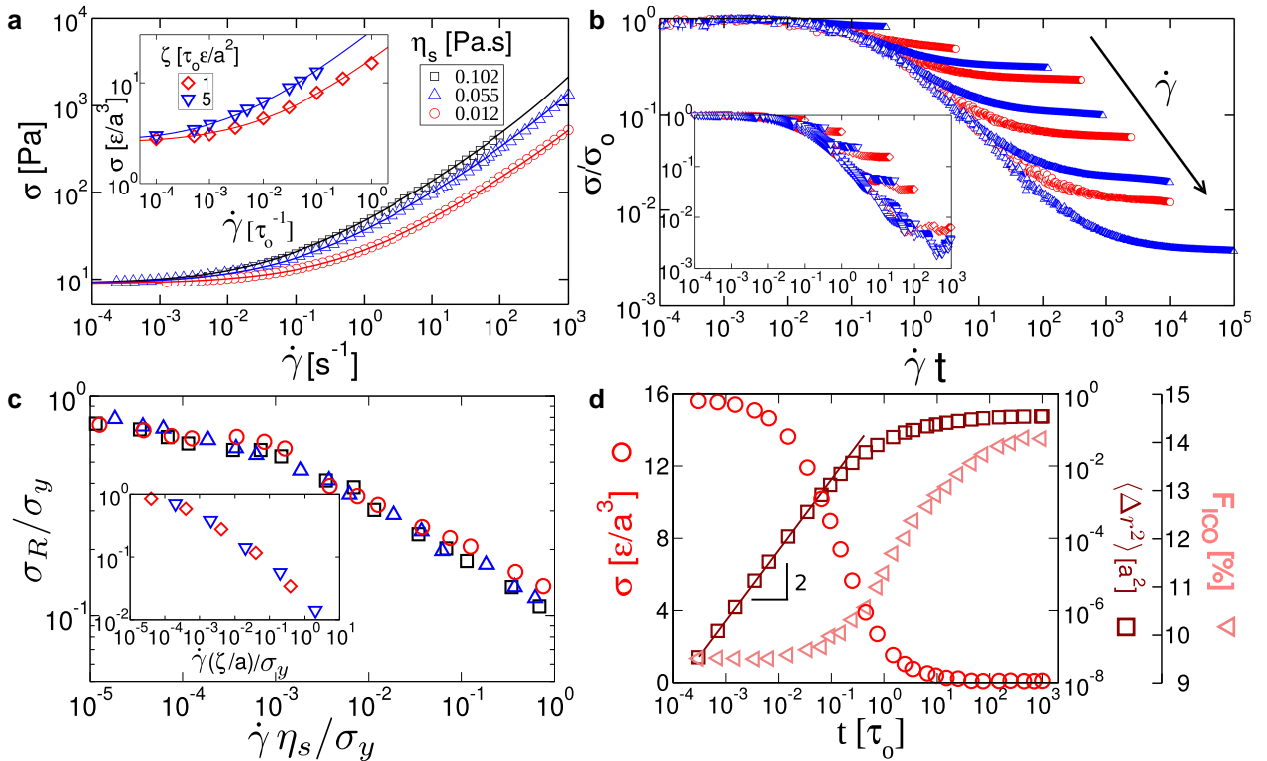

Fig. 1. Evidence of two distinct contributions governing stress relaxation upon flow cessation. a) Shear rate-dependent stress (flow curves). Main graph: experimental results obtained for different solvent viscosities. Lines through the data are fits to the three component model (17); the resulting yield stress is $\sigma_y = 8.9$ Pa. Inset: results obtained in simulations for two damping coefficients ζ. Lines through the data are fits to the Herschel–Bulkley model (2) fixing the yield stress value to $\sigma_y = 2.48\epsilon/a^3$, as obtained from quasistatic shear simulations. b) Stress relaxation upon flow cessation. The stress is normalized by the initial value σ_0 and the time is normalized with the inverse of the shear rate $\dot{\gamma}$. Main graph: selected experimental results obtained for $\eta_s = 0.055$ Pa s (blue triangles up) and $\eta_s = 0.012$ Pa s (red circles). From top to bottom the $\dot{\gamma} = 10^{-3}, 10^{-1}, 10^0, 10^1, 10^2$ s^{-1}. Inset: results obtained in simulations for $\zeta = 5$ $\tau_0\epsilon/a^2$ (blue triangles down) and $\zeta = 1$ $\tau_0\epsilon/a^2$ (red diamonds). From top to bottom $\dot{\gamma} = 10^{-4}, 10^{-3}, 10^{-2}, 10^{-1}, 10^0$ τ_0^{-1}. c) Residual stress normalized by the yield stress as a function of the viscous stress experienced during shear. Main graph: experimental results obtained for the three conditions described in a). Inset: results obtained in simulations for the two conditions described in the inset of a). d) Stress relaxation upon flow cessation for $\dot{\gamma} = 1.0$ τ_0^{-1} and $\zeta = 1$ $\tau_0\epsilon/a^2$ compared to the corresponding time dependences of the mean squared displacement $\langle \Delta r^2 \rangle$ and the fraction of Voronoi cells with icosahedral configuration F_{ICO}, where F_{ICO} at $t = 0$ corresponds to F_{ICO} reached under steady flow.

steady flow, and to subsequently measure stress relaxations while holding the strain constant. Consistent with previous work (6, 7, 9, 11), we find that the stress relaxation process upon flow cessation sensitively depends on the shear rate used to prepare the system. The higher the preshear rate the faster the stress relaxation and the lower the stress reached in the long-time limit of the stress relaxation test (see Fig. S3). Normalizing the stress by its initial value σ_o at $t = 0$s, and the time by the preshear rate, highlights an initial decay common to all flow conditions, independent of solvent viscosity, as shown in Fig. 1b. Such behavior indicates that the initial fast stress relaxation is not strictly related to a structural relaxation process that would require a significant relative displacement between neighboring particles, which should also depend on solvent viscosity.

At longer times, however, stress relaxation deviates from the unique behavior set by the preshear rate, the stress becoming eventually time-independent. This final stress plateau is commonly referred to as residual stress (7, 9, 11, 18) and reveals that elastic loading is never suppressed during shear. Indeed, a system subjected to a steady shear is forced to continuously reconfigure. However, in yield stress fluids, reconfiguration occurs intermittently, which allows for constant elastic reloading (14, 19–21). Naturally, as the strain is held constant during the flow cessation test, a net elastic load remains after the initially imbalanced local stresses relaxed below the local yield stresses (22–24). In contrast to the short-time relaxation, the residual stress is not solely set by the preshear rate. As denoted in Fig. 1b, preparing a system with a given shear rate will result in different residual stresses upon varying the solvent viscosity: the lower the solvent viscosity the larger the residual stress. The residual stress σ_R depends in fact on the viscous stress $\dot{\gamma}\eta_s$; indeed, reporting σ_R obtained at different viscosities as a function of $\dot{\gamma}\eta_s$ results in a unique master curve, as shown in Fig. 1c (for the unscaled data, see Fig. S3). Taking the residual stress as the relevant characteristic of the final stage of the stress relaxation process, the dependence on solvent viscosity indicates that the final stage involves a structural relaxation that requires the particles to reorganize with respect to each other and thus depends on viscous dissipation.

These findings clearly indicate that stress relaxation upon flow cessation depends on the shear parameters setting the flow conditions prior to flow cessation. To understand the microscopic origin of this dependence, we perform molecular dynamics simulations for a jammed packing of non-Brownian soft repulsive particles dispersed in an implicit solvent, in which they experience a drag force dependent on the solvent viscosity (25, 26). More detailed information on the numerical model and simulations is provided in Methods and Supplementary material. The characteristics of the flow curves and the flow cessation results obtained in the simulations with different drag coefficients ζ qualitatively agree with the experimental findings obtained at different η_s, as shown in the insets of Fig. 1a–c. In particular, the scaling behaviors denoted in the insets of Fig. 1b and c confirm that the short-time and long-time characteristics of stress relaxation are predominantly governed by respectively the shear rate and the viscous stress experienced during flow.

To gain a first microscopic understanding of these two distinct relaxation regimes, we characterize the particle dynamics during stress relaxation by determining the mean squared displacement $\langle\Delta r^2\rangle$, and we assess the structural evolution by decomposing the evolving particle packings into Voronoi cells, which enables us to determine the fraction of Voronoi cells that have an icosahedral shape, F_{ICO}. As shown in previous work (25–27), icosahedrally shaped Voronoi cells identify locally stiffer regions in particle

packings. The specific relevance of this particular structural parameter will be discussed later; for the current discussion, let us note that other structural parameters, like the mean number of particle contacts (6, 7), have been shown to display similar hallmarks in their temporal evolution as those observed in the temporal evolution of F_{ICO}.

As an example, we show the time dependence of F_{ICO} obtained at a high shear rate $\dot{\gamma} = 1\ \tau_0^{-1}$ and $\zeta = 1\ \tau_0\epsilon/a^2$, in comparison to the time dependence of respectively the mean squared displacement and the stress in Fig. 1d. Upon flow cessation, F_{ICO} remains essentially unchanged within a short-time interval, while the stress drops by about 30%. During this initial period the mean squared displacement increases with the square of time. This highlights that the initial relaxation, which solely depends on shear rate, independent of viscosity, is associated to quasiballistic motion without major changes in particle configuration. By contrast, a significant reorganization of the particle packing occurs in the final stage of stress relaxation. In absence of inertial effects (see Methods), the ballistic displacements can be ascribed to a partial release of particle contact deformations that were set during flow (19, 24). This quasielastic relaxation should be largely independent of the solvent viscosity, which is consistent with the initial scaling of the stress relaxation process discussed above (Fig. 1b).

More convincing evidence for the elastic origin of the initial stress relaxation is found, by analyzing the spatial configuration of the particle displacements, where we find that the particle displacements are not only directional, but also highly correlated. To illustrate this, we show as an example the spatial configuration of the displacement unit vectors observed within a sub-volume of the simulation box obtained for $\dot{\gamma} = 10^{-2}\ \tau_0^{-1}$ and $\zeta = 1\tau_0\epsilon/a^2$ in Fig. 2b; the time delay is here chosen to correspond to the time window over which we observe $\langle\Delta r^2\rangle \propto t^2$, marked by a vertical line in Fig. 2a, and the sub-volume chosen has a linear size of ≈ 4 particle diameters. To highlight the degree of correlation we assign a given color to the displacement vectors with the same pointing direction. Domains in which particles move along the same direction are clearly identified, supporting the idea that the process governing the initial stress relaxation relates to an elastic relaxation of contacting particles that have been compressed during shear flow (6, 7). Performing this analysis throughout the simulation box reveals that many such domains coexist, the direction of decompression changing from one domain to another. As a consequence, an analysis of the particle displacements along different directions yields that the overall particle displacements is isotropic, as shown in SI Fig. S3 and observed in previous investigations (6, 7).

To properly quantify the degree of alignment of the particle displacements, we determine a scalar order parameter S defined as the largest positive eigenvalue of the tensor obtained from the displacement directors, which is similar to the approach used to describe the degree of orientation in nematic liquid crystals (28). The value of S is zero when the unit vectors are randomly oriented and $S = 1$ when all unit vectors point in the same direction. This analysis is performed varying the linear size l_o of sub-volumes of the simulation box. As shown in Fig. 2c, S decreases with increasing l_o and saturates at 0.05 beyond $l_o = 12$. This fully supports our previous assessment, namely that the system contains correlated domains of finite size, the pointing direction of the displacement vectors differing from one domain to another.

The existence of dynamically correlated domains, observed upon flow cessation, raises the question of their origin and their dependence on shear rate. To address this question, we investigate the correlation in particle displacements at different shear
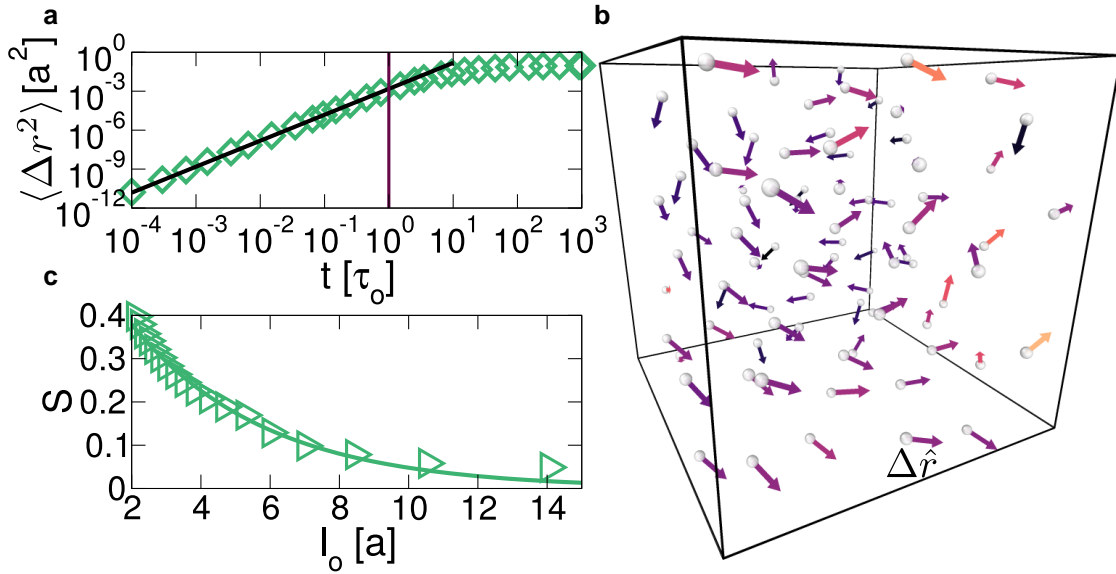
Fig. 2. Evidence of isotropically oriented domains of correlated dynamics. Example of spatial analysis of particle displacements upon flow cessation ($\dot{\gamma} = 10^{-2} \tau_o^{-1}$ and $\zeta = 1 \tau_o\epsilon/a^2$). a) Time dependence of mean squared displacement, the vertical line denoting the delay time used for the spatial analysis of the particle displacements. b) ($4a \times 4a \times 4a$) sub-volume of the simulation box showing the position of the particles center of mass upon flow cessation as a dot, the arrows representing the unit vectors of the subsequent particle displacements $\Delta\hat{r}$. The arrows are colored according to the unit vector direction. c) Scalar order parameter S as a function of the size of the sub-volume of the simulation box l_o. The continuous line corresponds to an exponential fit to the data, yielding a characteristic size for the domains in which the particles move in a given direction of $\approx 3.8a$.
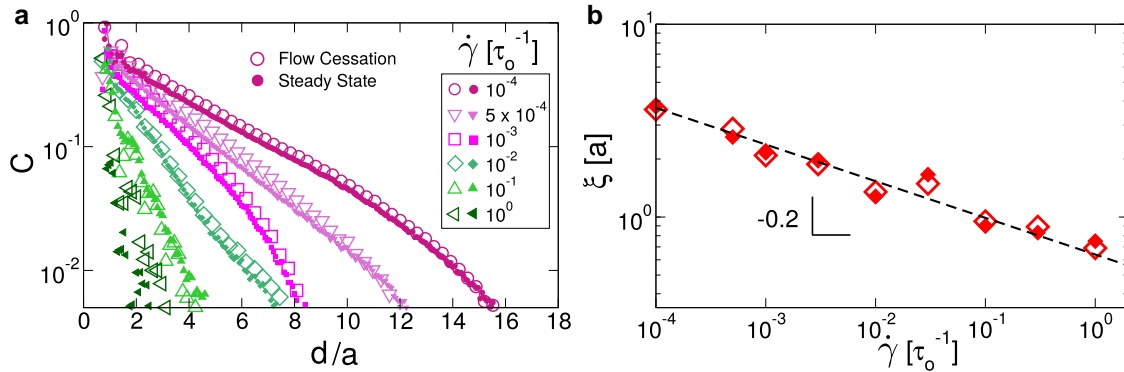

Fig. 3. Memory of spatial correlations of particle displacements. a) Selected examples of the spatial correlation function of dynamical fluctuations C obtained for $\zeta = 1 \tau_o\epsilon/a^2$. The closed symbols denote data obtained just before flow cessation and the open symbols denote the data obtained just after flow cessation. From top to bottom $\dot{\gamma} = 10^{-4}, 5 \times 10^{-4}, 10^{-3}, 10^{-2}, 10^{-1}, 10^0 \tau_o^{-1}$. b) Shear rate dependence of the correlation length determined from the decay rate of C. The dashed line is a power-law fit to the data with exponent -0.2.

rates. As we expect not only the displacement direction to be correlated but also the displacement magnitude, we determine for each particle i the magnitude of the displacement Δr_i observed within the time interval corresponding to that at which $\langle\Delta r^2\rangle \propto t^2$, and we assess its fluctuation over the average displacement, $\delta u_i = \Delta r_i - \langle\Delta r\rangle$. As a measure for correlation we then compute the spatial correlation function $C(d) = \frac{\langle\delta u_i \delta u_j\rangle}{\langle\delta u^2\rangle}$ for all pairs of particles i and j separated by a distance d (20, 29). This spatial correlation function strongly depends on the shear rate applied prior to flow cessation. Particles moving much more or much less than the average are correlated across a given distance, this distance being a decreasing function of the preshear rate, as shown in Fig. 3a (open symbols). Strikingly, an equivalent analysis of the spatial correlation of nonaffine particle displacements observed during shear flow reveals a direct correspondence between the dynamical correlations induced during shear flow and those observed upon flow cessation; as shown in Fig. 3a, $C(d)$ obtained for shear flow (closed symbols) almost perfectly superimpose $C(d)$

obtained for flow cessation (open symbols). Let us note, that for a given shear rate the delay time chosen to determine Δr_i is the same for both experiments, shear flow and flow cessation. Indeed, this delay time actually covers the time window for which $\langle\Delta r^2\rangle \propto t^2$ in both experiments, a quasiballistic motion being also observed in the nonaffine dynamics of the sheared system (19, 20).

The remarkable correspondence between dynamical correlations observed respectively during steady flow and upon flow cessation can be understood by considering that dynamics following flow cessation is a result of stress imbalances that are quenched in during flow. Within this framework, we postulate that stress fluctuations induced by correlated dynamics during flow are imprinted as stress imbalances upon flow cessation. These stress imbalances then serve as a source for dynamics during stress relaxation. Given that the spatial extent of stress fluctuations is set by the dynamically correlated domains during flow, the resulting stress imbalances driving correlated dynamics upon flow cessation reproduce the same correlation pattern. It is here worth

noticing that flow cessation tests effectively capture the exact imprint of the sheared states just before flow cessation. Indeed, repetitions of a given flow cessation test in independent simulation runs show that $C(d)$ varies at large d/a from one run to another, yet the excellent agreement between $C(d)$ obtained upon flow cessation and $C(d)$ obtained during flow is maintained, as long we compare the data collected just prior to and immediately after flow cessation (see Fig. S5). These observations underscore that subjecting jammed systems to a constant shear rate is akin to a training process, inherently encoding a memory of the sheared state through the presence of domains of correlated dynamics. Consequently, the flow cessation test can be used to gain information on the sheared state.

As denoted in Fig. 3a, the initial decay of $C(d)$ can be approximated by an exponential. This enables us to determine a dynamical correlation length ξ, from the decay rate of $C(d)$. Theories of nonlocal rheology and elastoplastic flow (30–36) predict the emergence of dynamical correlations, which are expected to grow as the shear stress approaches the dynamical yield stress. Direct evidence of such correlations has been so far missing but are directly revealed in our analysis. Broadly consistent with experiments (37) and simulations (38), we find that the shear rate dependence of ξ can be described by a power law with an exponent $\simeq -0.2$, as shown in Fig. 3b. This provides compelling evidence that subjecting a jammed system to a steady shear flow requires the system to break down into finite domains to accommodate the continuously increasing deformation, thereby releasing elastic stresses through localized plastic events, while storing stresses within the domains. Notably, the domain size increases with decreasing shear rate, indicating that the domains will essentially span the entire system as the shear rate goes to zero.

Based on our discussion so far, one may be inclined to assume that stress relaxation upon flow cessation is entirely governed by dynamical heterogeneities encoding stress imbalances during shear flow, these imbalances driving dynamics upon flow cessation until all local stresses dropped below the local yield stresses (22–24). However, shear flow does not only encode stress imbalances; it also alters the spatial particle configurations that need to adapt to the continuous flow. In particular, shear flow reduces the number of icosahedral configurations, i.e. the amount of locally stiffer regions.

As shown in Fig. 4a, the fraction of icosahedral Voronoi cells observed under steady shear flow F_{ICO}^S systematically decreases with increasing shear rate. Reminiscent of the scaling behavior observed for the residual stress, F_{ICO}^S scales with the viscous stress (for the unscaled data, see Fig. S6). The emerging picture is that the structural organization compatible with steady shear flow becomes increasingly incompatible with rigidity, i.e. mechanical stability at rest, as the viscous stress across the system increases. Consequently, the more the particle configuration has been altered with respect to that at rest, the more structural reorganization is needed to regain mechanical stability.

Indeed, for large enough viscous stresses, i.e. low enough F_{ICO}^S, F_{ICO} increases during stress relaxation, as denoted in Fig. 4b, where $F_{ICO}(t=0) = F_{ICO}^S$. Clearly, for stress relaxation to end after flow cessation, the system needs to regain a configuration compatible with a minimum rigidity, which appears to correspond to a minimal value of F_{ICO}. To assess this relation we determine the difference between the stress generated during flow and the residual stress $\Delta\sigma = \sigma_0 - \sigma_R$, and the corresponding difference between F_{ICO}^S and F_{ICO} obtained at the end of stress relaxation $\Delta F_{ICO} = F_{ICO}^S - F_{ICO}^{final}$. As shown in the inset of Fig. 4a, both quantities relate linearly to each other, which fully supports the idea that the magnitude of the residual stress is governed by conditions of mechanical stability that are well captured by the number of icosahedral configurations present in the system. Let us note that F_{ICO} does not evolve during stress relaxation if the preshear rates are low, such that F_{ICO}^S remains high enough. However, an inspection of the evolution of the structural configuration here reveals that, while F_{ICO} does not increase, the positions of the icosahedrally packed regions change during stress relaxation. This indicates that the actual arrangement of icosahedrally packed regions in space may be another factor determining the mechanical stability of the system at rest, consequently affecting the magnitude of residual stress. Such insight highlights outstanding questions to be the subject of future work.

In conclusion, our work discloses evidence of flow memory in jammed packings of soft spheres. At low shear rates, where the shear stress is of the order of the yield stress, memory is mainly encoded via dynamical correlations. Nonaffine particle displacements are directed and highly correlated setting long-range stress imbalances. These, in turn, trigger quasiballistic displacements upon flow cessation, with spatial correlations indistinguishable from those observed under flow. Upon increasing the shear rate, the range of correlated motion decreases, and the particle configurations evolve towards mechanically less stiff configurations.
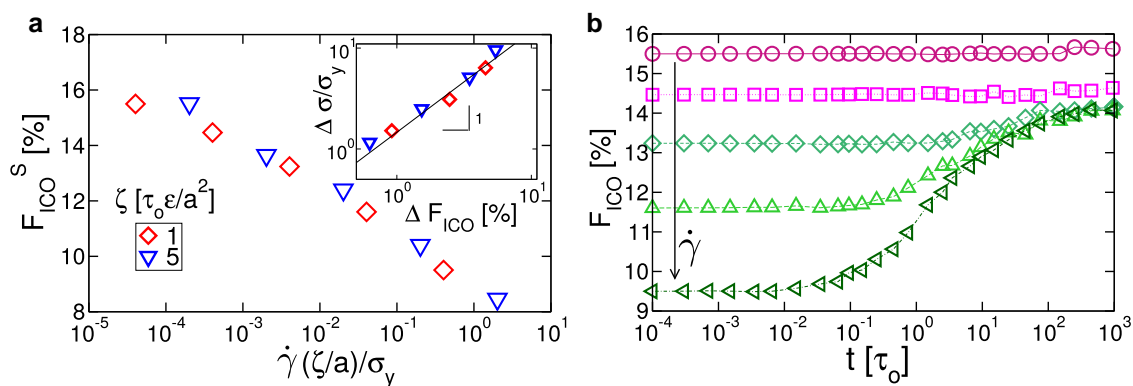

Fig. 4. Flow-induced weakening of particle configurations determining the magnitude of residual stresses upon flow cessation. a) Main graph: fraction of Voronoi cells with icosahedral configuration obtained during steady shear F_{ICO}^S as a function of the viscous stress normalized by the yield stress. Blue triangles down denote the data obtained for $\zeta = 5\,\tau_0\epsilon/a^2$, red diamonds denote the data obtained for $\zeta = 1\,\tau_0\epsilon/a^2$. Inset: magnitude of stress relaxation $\Delta\sigma$ normalized by the yield stress as a function of the magnitude of the changes in F_{ICO} observed after application of larger shear rates (see b). b) Temporal evolution of F_{ICO} upon flow cessation obtained for $\zeta = 1\,\tau_0\epsilon/a^2$. From top to bottom: the preshear rate is $\dot\gamma = 10^{-4}$, 10^{-3}, 10^{-2}, 10^{-1}, $10^0\,\tau_0^{-1}$.

The reduced stiffness facilitates stress relaxation upon flow cessation and entails an evolution of the local particle configurations towards a particle packing that is sufficiently rigid to warrant mechanical stability for stress relaxation to end. The two contributions determining stress relaxation upon flow cessation, namely local stress imbalances and unstable particle configurations, are the determining parameter at different time scales; the relaxation of elastically loaded contact forces is the main process determining stress relaxation at short time, while the rearrangements towards mechanically stable particle packings determine the long-time relaxation towards a residual stress.

Our work clearly exposes the microscopic origin of the relation between flow characteristics and stress relaxation upon flow cessation, and reveals how flow history is encoded into a soft jammed material.

Methods

Experiments

For experimental work, we use a dispersion of $2w\%$ Carbopol (974 p (Lubrizol)) in propylene glycol. The Carbopol consists of polyacrylic acid microgel aggregates, which are polydisperse in size, displaying a mean diameter of the order of $\approx 1\,\mu m$, as estimated from bright field microscopy images. Based on the development of the shear modulus as a function of concentration (see Fig. S1), we estimate the volume fraction of our sample to be $\approx 74\%$. More details on sample preparation and sample characteristics are given in Supplementary material.

Rheological experiments are performed with a commercial rheometer (Physica MCR 300) equipped with a cone and plate geometry (cone angle $1°$, cone truncation $52\,\mu m$). Cone and plate are both roughened to minimize wall slip. All rheological experiments are performed at respectively $10°C$, $20°C$, and $50°C$. Flow curves are determined by decreasing logarithmically the applied shear rate, while increasing logarithmically the averaging time per point to ensure steady flow conditions. Flow cessation experiments are performed for shear rates of multiples of $1\times$, $3\times$, $6\times$, of 10^{-3}, 10^{-2}, 10^{-1}, 10^{0}, 10^{1}, and 10^{2} s^{-1}. Prior to any flow cessation experiment, we prepare the sample in oscillatory shear at a frequency of 1Hz by performing an amplitude sweep, in which the strain amplitude is logarithmically decreased from 200% to 0.2% imposing 10 points per decade and a 10s equilibration time per point. This range of strain successively covers the nonlinear and linear range of elasticity, such that we presume that internal stresses are effectively minimized at the end of our preparation protocol (39). The results of the preparation experiment are also used to assess changes of the sample characteristics during long experiments, where we disregard experiments of an experimental series when the moduli have varied by more than 5% from the beginning of the series. Following the preparation protocol, the shear rate of interest is applied till the stress reaches steady state. The shear rate is then set to zero, and stress relaxations are recorded while the overall strain is maintained fixed. Because of tool inertia, $\dot{\gamma} = 0$ is only reached after a given time delay, a time delay that depends on the shear rate applied prior to imposing the cessation command on the rheometer. Taking this experimental limitation into account, we restrict the analysis of the stress relaxations to the time beyond this time delay.

Simulations

Our jammed suspension consists of non-Brownian polydisperse particles packed at volume fraction $\phi = 70\%$ with system size $N \approx 10^5$. The inter-particle interaction is the repulsive part of the shifted and truncated Lennard–Jones potential (40). Flow cessation simulations are performed on the steady state configurations at different rates $\dot{\gamma}$. The flow is stopped by setting the shear rate to zero, the strain is maintained, and the system is allowed to relax to a state that is in mechanical equilibrium. We solve the dissipative particle dynamics equation of motion, including a conservative force due to inter-particle interactions and a dissipative force due to the solvent viscosity ζ. All the physical quantities are expressed in terms of reduced units: mean particle diameter a is the distance unit, ϵ is the unit of energy, and the time unit is $\tau_o = \zeta a^2/\epsilon$, which is the time needed for a particle experiencing the drag ζ to move under a unit force ϵ/a over a distance a. The damping coefficients ζ are chosen such that m/ζ is at least $0.01\tau_o$ to ensure that the simulations are performed at overdamped conditions. Further details on generating steady state configurations are given in Section S2 and are fully discussed in Refs. (25, 41). Simulations are performed with Lees–Edwards periodic boundary conditions using LAMMPS (42). The stopping condition for the simulations is chosen such that the system's kinetic energy is $\approx 10^{-20}\epsilon$, corresponding to a total force per particle of $\approx 10^{-14}\epsilon/a$. We determine the stress relaxation processes and the stress of the final state for preshear rates ranging from 10^{-4} to $10^{0}\tau_o^{-1}$ and two damping coefficients $\zeta = 1$ and $5\tau_o\epsilon/a^2$.

The shear stress is computed by using the Virial formula $\hat{\sigma} = \frac{1}{V}\sum_{i\neq j}\vec{r}_{ij} \otimes \vec{f}_{ij}$, where V is the volume of the box, $\vec{r}_{ij}$ is the vector connecting the center of pairs (i, j), and $\vec{f}_{ij}$ is the force between the pairs. The mean squared displacement ($\langle \Delta r^2 \rangle$) is computed by $\langle \Delta r^2 \rangle = \langle \Delta x^2 + \Delta y^2 + \Delta z^2 \rangle$, where Δr is the particle displacement for a given time interval and the average is performed over all particles. The reference configurations used for computing the displacements after flow cessation are the steady flow configurations at the point of flow cessation. For the steady shear case, Δr is computed from the nonaffine displacements, obtained by removing the affine contributions from the particle displacement.

The scalar order parameter S is computed by using the displacement unit vectors $\hat{r}$, to determine the tensor $\mathbf{Q} = \frac{1}{2}\langle 3\Delta r_k \Delta r_l - \delta_{kl}\rangle$, with Δr_k denoting the component of the displacement unit vector, and the angular brackets $\langle\cdots\rangle$ signifying the average taken over all particle displacement unit vectors. The largest positive eigenvalue of $\mathbf{Q}$ is S.

The structural evolution during flow cessation is studied by performing Voronoi tessellation on the configurations using VORO++ library (43). From this analysis, we obtain the fraction of icosahedrons (12 faces, 30 edges, 20 vertices) present in the system, F_{ICO}.

Acknowledgments

Supplementary Material

Supplementary material is available at *PNAS Nexus* online.

Funding

Author Contributions

Data Availability

All data shown in the article and the Supplementary material are available on Zenodo: https://doi.org/10.5281/zenodo.11389467.

References

1 Nguyen QD, Boger DV. 1992. Measuring the flow properties of yield stress fluids. *Annu Rev Fluid Mech*. 24(1):47–88.

2 Bonn D, Denn MM, Berthier L, Divoux T, Manneville S. 2017. Yield stress materials in soft condensed matter. *Rev Mod Phys*. 89(3): 035005.

3 Balmforth NJ, Frigaard IA, Ovarlez G. 2014. Yielding to stress: recent developments in viscoplastic fluid mechanics. *Annu Rev Fluid Mech*. 46(1):121–146.

4 Nelson AZ, *et al.* 2019. Designing and transforming yield-stress fluids. *Curr Opin Solid State Mater Sci*. 23(5):100758.

5 Nicolas A, Ferrero EE, Martens K, Barrat J-L. 2018. Deformation and flow of amorphous solids: insights from elastoplastic models. *Rev Mod Phys*. 90(4):045006.

6 Mohan L, Bonnecaze RT, Cloitre M. 2013. Microscopic origin of internal stresses in jammed soft particle suspensions. *Phys Rev Lett*. 111(26):268301.

7 Mohan L, Cloitre M, Bonnecaze RT. 2015. Build-up and two-step relaxation of internal stress in jammed suspensions. *J Rheol (N Y N Y)*. 59(1):63–84.

8 Zakhari MEA, Hütter M, Anderson PD. 2018. Stress relaxation of dense spongy-particle systems. *J Rheol (N Y N Y)*. 62(4):831–843.

9 Ballauff M, *et al.* 2013. Residual stresses in glasses. *Phys Rev Lett*. 110(21):215701.

10 Sudreau I, *et al.* 2022. Residual stresses and shear-induced over-aging in boehmite gels. *Phys Rev Mater*. 6(4):L042601.

11 Vasisht VV, Chaudhuri P, Martens K. 2022. Residual stress in athermal soft disordered solids: insights from microscopic and mesoscale models. *Soft Matter*. 18(34):6426–6436.

12 Sudreau I, Manneville S, Servel M, Divoux T. 2022. Shear-induced memory effects in boehmite gels. *J Rheol (N Y N Y)*. 66(1):91–104.

13 Bandyopadhyay R, Mohan PH, Joshi YM. 2010. Stress relaxation in aging soft colloidal glasses. *Soft Matter*. 6(7):1462–1466.

14 Song J, *et al.* 2022. Microscopic dynamics underlying the stress relaxation of arrested soft materials. *Proc Natl Acad Sci U S A*. 119(30):e2201566119.

15 Hendricks J, *et al.* 2019. Nonmonotonic stress relaxation after cessation of steady shear flow in supramolecular assemblies. *Phys Rev Lett*. 123(21):218003.

16 Chen Y, Rogers SA, Narayanan S, Harden JL, Leheny RL. 2020. Microscopic dynamics of stress relaxation in a nanocolloidal soft glass. *Phys Rev Mater*. 4(3):035602.

17 Caggioni M, Trappe V, Spicer PT. 2020. Variations of the Herschel–Bulkley exponent reflecting contributions of the viscous continuous phase to the shear rate-dependent stress of soft glassy materials. *J Rheol (N Y N Y)*. 64(2):413–422.

18 Cuny N, Bertin E, Mari R. 2022. Dynamics of microstructure anisotropy and rheology of soft jammed suspensions. *Soft Matter*. 18(2):328–339.

19 Khabaz F, Cloitre M, Bonnecaze RT. 2020. Particle dynamics predicts shear rheology of soft particle glasses. *J Rheol (N Y N Y)*. 64(2): 459–468.

20 Vasisht VV, Dutta SK, Del Gado E, Blair DL. 2018. Rate dependence of elementary rearrangements and spatiotemporal correlations in the 3D flow of soft solids. *Phys Rev Lett*. 120(1):018001.

21 Hwang HJ, Riggleman RA, Crocker JC. 2016. Understanding soft glassy materials using an energy landscape approach. *Nat Mater*. 15(9):1031–1036.

22 Puosi F, Olivier J, Martens K. 2015. Probing relevant ingredients in mean-field approaches for the athermal rheology of yield stress materials. *Soft Matter*. 11(38):7639–7647.

23 Barbot A, *et al.* 2018. Local yield stress statistics in model amorphous solids. *Phys Rev E*. 97(3):033001.

24 Cuny N, Mari R, Bertin E. 2021. Microscopic theory for the rheology of jammed soft suspensions. *Phys Rev Lett*. 127(21):218003.

25 Vasisht VV, Del Gado E. 2020. Computational study of transient shear banding in soft jammed solids. *Phys Rev E*. 102(1):012603.

26 Vasisht VV, Roberts G, Del Gado E. 2020. Emergence and persistence of flow inhomogeneities in the yielding and fluidization of dense soft solids. *Phys Rev E*. 102(1):010604.

27 Pinney R, Liverpool TB, Royall CP. 2016. Structure in sheared supercooled liquids: dynamical rearrangements of an effective system of icosahedra. *J Chem Phys*. 145(23):234501.

28 Chaikin PM, Lubensky TC, Witten TA. 1995. *Principles of condensed matter physics*. Vol. 10. Cambridge: Cambridge University Press.

29 Weeks ER, Crocker JC, Weitz DA. 2007. Short- and long-range correlated motion observed in colloidal glasses and liquids. *J Phys Condens Matter*. 19(20):205131.

30 Picard G, Ajdari A, Bocquet L, Lequeux F. 2002. Simple model for heterogeneous flows of yield stress fluids. *Phys Rev E*. 66(5): 051501.

31 Goyon J, Colin A, Ovarlez G, Ajdari A, Bocquet L. 2008. Spatial cooperativity in soft glassy flows. *Nature*. 454(7200):84–87.

32 Bocquet L, Colin A, Ajdari A. 2009. Kinetic theory of plastic flow in soft glassy materials. *Phys Rev Lett*. 103(3):036001.

33 Mansard V, Colin A. 2012. Local and non local rheology of concentrated particles. *Soft Matter*. 8(15):4025–4043.

34 Ferrero EE, Martens K, Barrat J-L. 2014. Relaxation in yield stress systems through elastically interacting activated events. *Phys Rev Lett*. 113(24):248301.

35 Lin J, Lerner E, Rosso A, Wyart M. 2014. Scaling description of the yielding transition in soft amorphous solids at zero temperature. *Proc Natl Acad Sci U S A*. 111(40):14382–14387.

36 Benzi R, *et al.* 2019. Unified theoretical and experimental view on transient shear banding. *Phys Rev Lett*. 123(24):248001.

37 Jop P, Mansard V, Chaudhuri P, Bocquet L, Colin A. 2012. Microscale rheology of a soft glassy material close to yielding. *Phys Rev Lett*. 108(14):148301.

38 Clemmer JT, Salerno KM, Robbins MO. 2021. Criticality in sheared, disordered solids. I. Rate effects in stress and diffusion. *Phys Rev E*. 103(4):042605.

39 Lidon P, Villa L, Manneville S. 2017. Power-law creep and residual stresses in a carbopol gel. *Rheol Acta*. 56(3):307–323. doi:10.1007/s00397-016-0961-4

40 Weeks JD, Chandler D, Andersen HC. 1971. Role of repulsive forces in determining the equilibrium structure of simple liquids. *J Chem Phys*. 54(12):5237–5247.

41 Shrivastav GP, Chaudhuri P, Horbach J. 2016. Heterogeneous dynamics during yielding of glasses: effect of aging. *J Rheol (N Y N Y)*. 60(5):835–847.

42 Plimpton S. 1995. Fast parallel algorithms for short-range molecular dynamics. *J Comput Phys*. 117(1):1–19.

43 Rycroft C. 2009. Voro++: a three-dimensional voronoi cell library in C++. Technical report, Lawrence Berkeley National Lab.(LBNL), Berkeley, CA (United States).